

Mechanisms linking multi-year La Niña with preceding extreme El Niño

Tomoki Iwakiri (✉ iwakiri@ori.u-tokyo.ac.jp)

Atmosphere and Ocean Research Institute, The Unive <https://orcid.org/0000-0003-3943-0967>

Masahiro Watanabe

University of Tokyo <https://orcid.org/0000-0001-6500-2101>

Article

Keywords: El Niño, La Niña,

Posted Date: December 28th, 2020

DOI: <https://doi.org/10.21203/rs.3.rs-123982/v1>

License:   This work is licensed under a Creative Commons Attribution 4.0 International License.

[Read Full License](#)

Version of Record: A version of this preprint was published at Scientific Reports on August 25th, 2021.
See the published version at <https://doi.org/10.1038/s41598-021-96056-6>.

Abstract

El Niño/La Niña, characterized by anomalous sea surface temperature warming/cooling in the central-eastern equatorial Pacific, is a dominant interannual variability with irregularity, impacting worldwide weather and socioeconomics. The observed records show that La Niña often persists for more than two years, called “multi-year La Niña” which tends to accompany extreme El Niño in the preceding year; however, the physical linkage between them remains unclear. Here we show using reanalysis data that an extreme El Niño excites atmospheric conditions that favor the generation of the multi-year La Niña in subsequent years. Easterly wind anomalies along the northern off-equator in the Pacific during the decay phase of an extreme El Niño are crucial. They act to discharge ocean heat content (OHC) via an anomalous northward Ekman transport; the negative OHC anomaly is large enough to be restored by a single La Niña and, therefore, causes another La Niña to occur in the second year. Furthermore, analyses of the Coupled Model Intercomparison Project Phase 6 (CMIP6) models show that the occurrence frequencies of multi-year La Niña and extreme El Niño are highly correlated, supporting the abovementioned mechanism. Our results provide physical evidence that the increasing frequency of multi-year La Niña is explained by the increasing El Niño amplitude since the late 20th century.

Introduction

The El Niño-Southern Oscillation (ENSO) is a quasi-periodic variability with irregularity in several aspects such as amplitude and transition, and the life cycle is known to be locked with seasonal march: growing in boreal spring and summer, maturing in winter, and decaying in the following spring¹⁻³. The oscillatory nature of ENSO has been well explained by the linear theory called the recharge oscillator paradigm, in which equatorial Pacific warm water volume anomalies can be used as a harbinger of the ENSO sea surface temperature (SST) anomaly⁴⁻⁶. According to this theory, the transition from La Niña event to El Niño event occurs such that the intensified easterly trade winds associated with the La Niña SST anomaly act to recharge warm subsurface water from the off-equator to the equatorial strip via a slow Sverdrup adjustment. The deepened thermocline weakens the cooling effect due to mean upwelling, referred to as the thermocline feedback, which diminishes the La Niña SST anomaly and, then, causes ENSO turnabout. This process has been verified using a phase relationship between the observed warm water volume anomaly in the equatorial Pacific and the Niño 3.4 SST anomaly⁷⁻⁹.

In reality, the temporal behavior of ENSO is highly complex¹⁰. Unlike solutions in the recharge oscillator equations, observations show that ENSO has a strong transition asymmetry; El Niño terminates rapidly but La Niña often lasts more than two years, the latter referred to as multi-year La Niña¹¹. In particular, extremely strong El Niño events tend to terminate and transition to La Niña within one year. When extreme El Niño decays from winter to spring, equatorial westerly wind anomalies are known to shift southward¹², causing equatorial thermocline shoaling and contributing to the rapid termination of extreme El Niño¹³⁻¹⁵. This atmospheric pattern with southward-shifted westerly anomalies is induced by a nonlinear

coupling between ENSO's interannual frequency and the annual cycle in the western Pacific, known as a combination mode (C-mode)^{16–18}.

The multi-year persistency of La Niña has been investigated using observations and climate model simulations. A key process for the ENSO phase transition is the delayed negative thermocline feedback (equivalent to the recharge/discharge process), which is weak for La Niña and may, therefore, explain the longer duration of La Niña than El Niño¹⁹. A report also states that the SST anomaly pattern has a wide meridional structure when La Niña persists for more than two years²⁰. Because the recharge after the peak of La Niña is effective with a narrow meridional structure of the wind stress curl, the difference in the SST pattern may contribute to the multi-year persistency of La Niña. In addition, remote influence from the Atlantic and Indian Ocean may play a role in the multi-year persistence of La Niña that was predicted out to two years ahead in a model²¹. A common suggestion from previous studies is that a multi-year La Niña tends to occur after an extreme El Niño. A recent study shows that the duration of La Niña is strongly influenced by the amplitude of the preceding El Niño in both observations and a long climate model simulation, presumably due to a large initial discharge²². However, the physical link between extreme El Niño and the subsequent multi-year persistence of La Niña has not been comprehensively examined using ocean subsurface reanalysis data. Furthermore, extremely strong El Niño events decay rapidly owing to a coupling with the annual cycle¹⁷; however, the influence of the rapid termination of El Niño on the occurrence of multi-year La Niña is unclear.

In this study, we address the following questions: What process distinguishes multi-year and single-year La Niña? Is there a dynamical connection between extreme El Niño and a subsequent multi-year La Niña? By answering these questions, we identified triggers for multi-year La Niña. In addition to the observational analyses, we investigated the connection between extreme El Niño and multi-year La Niña in 37 CMIP6 models and demonstrated that their observed physical linkage is consistently seen in the climate model ensemble. There are several reports that a multi-year La Niña in the first and second years has distinct impacts on the atmospheric circulation over North America and East Asia^{11,23,24}. Although ENSO forecasting for more than one year is still challenging^{25,26}, deepening our understanding of the mechanism of a multi-year La Niña and its connection to a preceding extreme El Niño would help improve seasonal and long-term climate prediction.

Results

Time evolution of two types of La Niña

We identify six and four multi-year and single-year La Niña, respectively, using the observed Niño 3.4 SST anomaly (hereafter N3.4) during 1961–2016 (Supplementary Fig. 1). We define the period when the first La Niña develops as Year (0) in the composite analysis. By taking composites for these events of N3.4 and the ocean heat content (OHC) integrated over the equatorial Pacific (OHC_{eq}: 120° E–60° W, 5.5° S–5.5° N, surface–500 m), the latter measuring the equatorial Pacific warm water volume, trajectories

Loading [MathJax]/jax/output/CommonHTML/jax.js

associated with the two types of La Niña are obtained in the phase space (Fig. 1a). The composite-mean trajectories are akin to the limit cycle^{4,7}, showing that La Niña in Year (0) follows El Niño in Year (-1), both of which reach their peak in boreal winter (November–December–January: NDJ, circles in Fig. 1a). Four out of six multi-year La Niña events accompany extreme El Niños (the NDJ-mean N3.4 exceeding the 1.5 standard deviation) in the preceding year, whereas all El Niño before a single-year La Niña has a moderate amplitude (Supplementary Fig. 1). Consistent with the recharge theory, the OHC_{eq} anomaly lead N3.4 by 2–3 months and peaks in September–October–November (SON) before the mature phase of La Niña. While the positive OHC_{eq} anomaly during SON(-1) is comparable in magnitude between the two composites, the negative OHC_{eq} anomaly in SON(0) preceding multi-year La Niña is four times as large as that of single-year La Niña. Despite the large difference in the OHC_{eq} anomaly, the negative N3.4 in NDJ(0/1) in the multi-year composite is only 1.3 times larger than that in the single-year composite due to a strong asymmetry in the thermocline feedback and nonlinear dynamical heating, which suppresses La Niña but enhances El Niño^{7,27,28}. This contrast in magnitude between the SST and OHC_{eq} anomalies is also an important feature of multi-year La Niña and may contribute to the recurrence of La Niña.

After NDJ(0/1), the negative OHC_{eq} anomaly eventually turns positive in the single-year composite, leading to the termination of La Niña. In contrast, the OHC_{eq} anomaly in the multi-year composite decays but remains negative until the following year, resulting in an intensified subsequent La Niña in NDJ(1/2). The time evolution shown in Fig. 1a indicates that the recurrence of La Niña is consistent with the linear recharge oscillator theory. An exceedingly negative OHC_{eq} anomaly in NDJ(0/1) that is not restored within a year is crucial in understanding multi-year La Niña²². The spatial distribution of composite OHC anomalies in its peak season, SON(0), is shown in Fig. 1b,c. The multi-year composite is characterized by a contrast between large negative OHC anomalies in the equatorial Pacific and positive anomalies in the western-central Pacific at approximately 5°–15° N, suggesting that the former was induced by a mass exchange between the equatorial strip and northern off-equator. Such an equatorial asymmetry is not observed in the single-year composite, which indicates weak negative OHC anomalies in the central-eastern equatorial Pacific and positive anomalies in the tropical western Pacific.

Physical link between multi-year La Niña and preceding extreme El Niño

A significant difference between multi-year and single-year La Niña is clearly observed in the composite time series of N3.4 and OHC_{eq} anomalies (Fig. 2a,b). To clarify the processes responsible for the strong discharge of warm water during the growth phase of multi-year La Niña, heat budget analysis was performed on OHC_{eq} using ocean reanalysis datasets (Methods). We present the result based on ORAS4 in Fig. 2b-d because the budget terms reveal the smallest error among the four reanalysis data; however, our conclusion depends little on the dataset (Supplementary Fig. 2).

A large negative OHC_{eq} anomaly in SON(0) for the multi-year La Niña composite occurs because of a large negative OHC_{eq} tendency during the first half of Year (0), i.e., from February to June, denoted as FMAMJ(0) (black solid curve in Fig. 2c). For both multi-year and single-year La Niña composites, the aggregated OHC_{eq} budgets (shading in Supplementary

Fig. 2a,e), which can then be decomposed into individual terms (zonal and meridional advection terms due to geostrophic and Ekman currents, heat exchange at the bottom of the subsurface, and net heat flux at the surface). The sum of the geostrophic and Ekman terms (i.e., Sverdrup heat transport) is called the recharge rate, which explains most of the OHC_{eq} tendency (green curves in Fig. 2c). Unlike the linear recharge oscillator theory, the composited recharge rate indicates a persistent large negative anomaly during FMAMJ(0) when the N3.4 signal is weak.

The decomposition of the recharge rate into components of surface Ekman current heat transport (EHT) and geostrophic current heat transport (GHT) is shown in Fig. 2d. On the one hand, the GHT during the peak period of the preceding El Niño shows a large negative anomaly in the multi-year composite compared to the single-year composite; however, they are similar after scaling with N3.4 (Supplementary Table 1). This implies that the GHT-induced discharge is not a primary factor for generating the OHC_{eq} difference between multi-year and single-year La Niña. On the other hand, EHT in the multi-year composite becomes negative in FMAMJ(0) and contributes to the large negative recharge rate (i.e., discharge); hence, a large negative OHC_{eq} tendency is not observed in the single-year composite (Fig. 2c). The composite heat transport at the northern and southern boundaries indicates that the strong discharge for multi-year La Niña in FMAMJ(0) is attributed to EHT across the northern boundary, which is slightly weakened by the heat imported across the southern boundary (Supplementary Fig. 3). In general, GHT is inversely proportional to N3.4 throughout the year and primarily represents the recharge theory, while EHT has a similar magnitude to GHT but is proportional to N3.4 from the summer to late autumn, indicating that this process disturbs a theoretical recharge/discharge (Supplementary Fig. 4c–f). Consequently, the recharge rate is not correlated with N3.4 during the summer (Supplementary Fig. 4a,b).

During FMAMJ(0) corresponding to the transition period from El Niño to La Niña, composite anomalies of SST, precipitation, and surface wind stress show different patterns between multi-year and single-year La Niña (Fig. 3). The El Niño SST pattern persists in the multi-year La Niña composite but transforms to a weak La Niña pattern in the single-year composite (Fig. 3a,c) because strong El Niño tend to last several more months compared to weak El Niño²². In the multi-year composite map, anomalous positive precipitation is found to the south of the equator, while negative precipitation anomalies appear along the northern off-equator. This southward shift of the precipitation anomaly pattern has been identified during the decay phase of extreme El Niño and is because the climatological mean SST distribution shifted southward in this season¹⁶. Consistently, eastward wind stress anomalies are present over the south of the equator, whereas westward anomalies dominate over the northern off-equator, the latter being responsible for the strong EHT-induced discharge (Fig. 3b). The anomalous cross-equatorial wind stresses can form in response to diabatic heating anomalies associated with the southward-shifted precipitation anomaly pattern shown in Fig. 3a (Supplementary Fig. 5a,b). Overall, anomaly patterns in precipitation and wind stress in the multi-year composite are consistent with the equatorial asymmetric distribution of OHC anomalies during SON(0) (Fig. 1b). The atmospheric responses are similar to the C-mode, which acts to terminate extreme El Niño^{13,18}, supporting links with a preceding extreme El Niño.

The single-year composite maps lack anomalous zonal wind stresses over the off-equator, likely due to weak, symmetric precipitation anomalies around the equator (Fig. 3c, d).

Exceptional cases of coupling between extreme El Niño and multi-year La Niña exist. Yet, the importance of the easterly wind stress anomaly over the northern off-equator for multi-year La Niña is commonly identified. Two out of six multi-year La Niña events (1970–72 and 2007–09) are preceded by moderate but not extreme El Niño (Supplementary Fig. 6). Composite SST and precipitation anomalies for these two events are almost similar to those of the composites of single-year La Niña. However, the anomalous easterly wind stresses appear over the northern off-equator as a response to thermal forcing in the equatorial Pacific (Supplementary Fig. 5c,d; Supplementary Fig. 6c, d). In addition, two out of six extreme El Niño events (1965–66 and 1991–92) do not accompany a multi-year La Niña (Supplementary Fig. 7). The composite anomalies for these two El Niño events show that the negative OHC_{eq} anomaly is weak in Year (0/1). Consistently, easterly wind stress anomalies are absent along the northern off-equator during FMAMJ(0). These results confirm that the anomalous easterly winds and associated EHT-induced discharge in the northern off-equatorial latitudes link multi-year La Niña with a preceding El Niño.

Analysis of CMIP6 control simulations

To obtain a robust relationship between extreme El Niño and multi-year La Niña, we repeated our analyses in 500-year long preindustrial control simulations using 37 Earth system models (ESMs) participating in CMIP6²⁹ (Supplementary Table 2). First, we evaluated the ability of ESM to generate multi-year La Niña defined for each model (Methods). The ratio of the number of multi-year events against the total number of La Niña, 0.60 for 1961–2016 and 0.48 for 1901–2018 in observations, varies across models at 0.28 ± 0.13 (the range denotes the inter-model standard deviation). On average, multi-year La Niña occur less frequently in ESMs than in observations; however, some models capture the observed frequency of multi-year events. As expected, a significant positive correlation ($r = 0.62$) is found between the frequencies of multi-year La Niña and extreme El Niño in CMIP6 models (Fig. 4a). This indicates that multi-year La Niña tend to occur more often in a model that generates many extreme El Niño, supporting a physical link between them.

We calculate the ratio of the number of multi-year La Niña events accompanying preceding extreme El Niño against the total number of multi-year La Niña events. This ratio, denoted as R_{E-L} , measures the coupling between extreme El Niño and multi-year La Niña (Fig. 4b). The observed values of R_{E-L} are 0.67 for 1961–2016 and 0.40 for 1901–2018, indicating an enhanced coupling between multi-year La Niña and extreme El Niño since the late 20th century. The multi-model ensemble (MME) mean estimate of R_{E-L} is similar to the observed value for 1901–2018; however, R_{E-L} in the ensemble varies considerably across models. Interestingly, R_{E-L} is significantly correlated with the ENSO amplitude measured by the standard deviation of N3.4 ($r = 0.59$ for the entire ensemble). Indeed, the average ENSO amplitude in ten highest R_{E-L} models is approximately 50% larger than the average amplitude in ten lowest R_{E-L} models (1.13 ± 0.24 K versus 0.76 ± 0.25 K). This relationship can be understood given that a frequent occurrence of extreme El Niño which increase both the overall ENSO amplitude and frequency of multi-

year La Niña. Thus, the analysis of CMIP6 models supports the physical mechanism linking extreme El Niño with multi-year La Niña. An increase in observed R_{E-L} in the late 20th century may also be related to an increase in ENSO amplitude.

Implications for ENSO dynamics

In this study, we examined the mechanisms of multi-year La Niña which occupies two third of La Niña events during the period 1961–2016. A physical link was determined between multi-year La Niña and extreme El Niño, of which the latter often accompanied in the preceding year. The essential mechanism for the transition from an extreme El Niño to multi-year La Niña is explained by a modification of the recharge/discharge cycle, which is schematically illustrated in Supplementary Fig. 8. Using composite analyses of observations and reanalysis data, we found that significant negative OHC anomalies form in the equatorial Pacific during the first La Niña and they persist after its peak. This strong mass discharge of the upper ocean cannot be restored by a single La Niña and, therefore, causes another La Niña to occur in the second year. The large negative OHC anomaly before the peak of the first La Niña is induced by intensified northward Ekman heat transport driven by surface easterly anomalies along the northern off-equator. The patterns of surface wind stress anomalies, easterly anomalies to the north, and westerly anomalies to the south of the equator have occurred when extreme El Niño decays. This plays a central role in linking extreme El Niño with subsequent multi-year La Niña.

Given that ENSO is positively skewed^{27,28,30}, i.e., El Niño is stronger than La Niña, it is reasonable to doubt that multi-year La Niña is an apparent feature arising from the climatological mean shifted toward El Niño due to amplitude asymmetry. However, our results clearly show that multi-year La Niña is not a statistical artefact but a part of the intrinsic complex nature of ENSO. Previous studies have shown the contribution of anomalous wind stress curl causing GHT in the ENSO transition^{9,20,31–33}, an active role of inter-basin interaction for the transition asymmetry³⁴, and a meridional shift of westerly surface wind anomalies for the transition from extreme El Niño to La Niña^{12–14,35}. Although we do not exclude these processes during ENSO phase transition, we demonstrate that the anomalous Ekman heat transport is crucial to transition from extreme El Niño to multi-year La Niña. The link between extreme El Niño and multi-year La Niña as represented by R_{E-L} is robust; therefore, the occurrence of multi-year La Niña may be predictable beyond the typical predictability of ENSO events³⁶. If a coupled atmosphere-ocean model initialized with an extreme El Niño condition can reproduce the wind stress pattern responsible for the anomalous Ekman heat transport, the subsequent two years, when a multi-year La Niña will occur, maybe predicted owing to the large memory in the ocean heat content^{21,37}. Regarding long-term changes in ENSO properties, we demonstrated that multi-year La Niña occurred frequently during 1961–2016 compared to previous decades. This is consistent with an increasing ENSO amplitude and, hence, frequent extreme El Niño since the late 20th century³⁸. Since ENSO is suggested to be amplified in a warming climate, multi-year La Niña may be observed more frequently as global warming continues³⁹.

Methods

Loading [MathJax]/jax/output/CommonHTML/jax.js

Observations and reanalysis data

We used the observed monthly SST and precipitation datasets from COBE-SST2⁴⁰ and PRECipitation REConstruction (PREC)⁴¹ of the National Oceanic and Atmospheric Administration, respectively. Four ocean reanalysis products that contain temperature, salinity, current velocity, and surface heat flux were also used: Ocean Reanalysis System 4 (ORAS4)⁴², Ocean Reanalysis System 5 and its backward extension (ORAS5)⁴³, German contribution to the consortium for Estimating the Circulation and Climate of the Ocean system 2 (GECCO2)⁴⁴, and Geophysical Fluid Dynamics Laboratory Ensemble Coupled Data Assimilation version 3.1 (GFDL-ECDAv3.1)⁴⁵. For the atmospheric fields, we used combined data of ERA-40⁴⁶ and ERA-Interim⁴⁷, which were adopted for surface forcing in producing ORAS4. The analysis period was from January 1961 to December 2016, and de-trended anomalies were defined as deviations from monthly climatology calculated for the 30-year period from 1981 to 2010.

CMIP6 multi models

We used preindustrial control simulations from 37 CMIP6 coupled global climate models²⁹ (listed in Supplementary Table. 2) to analyze monthly SST (variable name: “tos”). While each model was integrated for different periods, we used the first 500 years for the analysis. De-trended anomalies are defined as deviations from monthly climatology calculated for the entire period.

Detection of ENSO events

Detection of ENSO events (extreme El Niño; single- and multi-year La Niña) is based on the three-month running mean time series of SST anomalies averaged in the Niño 3.4 region (170° W–120° W, 5° S–5° N; denoted as N3.4). La Niña is defined when N3.4 is below -0.5 K in its peak season (NDJ in observations). When the La Niña persists for two consecutive years, it is classified as a multi-year La Niña. El Niño is defined when N3.4 is above 0.5 K, and is categorized as extreme El Niño when N3.4 exceeds 1.5 standard deviation (1.27 K for COBE-SST2 in 1961–2016). We did not analyze the 2015/16 extreme El Niño because the observational record ended in December 2016. We extracted six multi-year and four single-year La Niña events for the period 1961–2016 (Supplementary Fig. 1). All La Niña events were preceded by El Niño. When the multi-year La Niña lasted for three years, we analyzed the first two years. For the CMIP6 multi-model analysis, the threshold to detect El Niño/La Niña was 0.7 standard deviation, which is 0.5 K in COBE-SST2 for the period 1901–2018, but corresponds to a different value in a different model.

Ocean heat budgets

To quantify the processes that give rise to a large anomaly in OHC_{eq} during multi-year La Niña, we calculated ocean heat budgets for the equatorial area where OHC_{eq} was defined (120° E–60° W, 5.5° S–5.5° N and from the surface to 500 m).

$$\frac{\partial \langle H \rangle}{\partial t} = - \underbrace{\int_{5.5^{\circ}N} \rho C_p T \cdot v \, dS + \int_{5.5^{\circ}S} \rho C_p T \cdot v \, dS}_{\text{Recharge rate}} + \int_{120^{\circ}E} \rho C_p T \cdot u \, dS + \int_{500m} \rho C_p T \cdot w \, dS + \int_{\text{surface}} Q \, dS \quad (1)$$

where H indicates OHC; T is ocean temperature; and u , v , and w are the ocean zonal, meridional, and vertical currents, respectively. ρ and C_p are the seawater density and specific heat of the ocean, respectively. Q is the net surface heat flux. The bracket $\langle \dots \rangle$ represents the integral of the entire domain. S is the cross-sectional area of each boundary. The terms on the RHS represent ocean heat transport across boundaries, defining inward positive. The sum of the first two terms in Eq. (1) indicates heat exchanges across meridional boundaries, defining the recharge rate (i.e., Sverdrup heat transport). The third and fourth terms represent the heat exchange across the western and bottom boundaries, and the last term is the net heat gain/loss at the ocean surface. We used monthly mean data from the atmosphere and ocean reanalysis datasets for calculating the budget terms and confirmed that the sum of the RHS terms matches with the OHC_{eq} tendency well (Supplementary Fig. 2). The OHC_{eq} defined in this study is highly correlated with the warm water volume in the equatorial Pacific ($r = 0.92$)⁷.

The recharge rate can be decomposed into contributions from surface Ekman current heat transport (EHT) and geostrophic current heat transport (GHT). We estimated EHT following the Ekman theory⁴⁸ as

$$\text{EHT} = -C_p \int_0^L \frac{\tau_x}{f} T_E \, dx, \quad (2)$$

where τ_x is the zonal wind stress. f is the Coriolis parameter, and L is the basin width. The mean velocity-weighted temperature over the Ekman layer, T_E , is calculated as

$$T_E = \sum v_n(z)T(x, y, z), \quad (3)$$

$$v_n \propto e^{z/\delta} \sin\left(\frac{-z}{\delta} + \frac{\pi}{4}\right), \quad (4)$$

where v_n is a normalized velocity weight as a function of ocean depth, z . The Ekman layer depth, δ , is assumed to be constant at 70 m, which is not sensitive to the different values, such as 50 or 100 m. The contribution from GHT is the difference between the recharge rate and the EHT term.

Diagnosing steady atmospheric response to an imposed heating

We diagnosed a thermally forced steady atmospheric response using a linear baroclinic model (LBM)⁴⁹. The model has a horizontal resolution of T42 and 20 vertical levels. The basic states, FMAMJ climatology, and anomalous diabatic heating (including condensational heating, radiative heating, surface heat flux, and subgrid-scale heat flux convergences)⁵⁰ were calculated using the combined data of ERA40 and ERA-Interim. For simplification, the thermal forcing was confined to the tropical Pacific (120° E–80° W, 30° S–30° N).

Statistical significance

We applied a two-sided Student's t-test for the composite and correlation analyses, and Welch's t-test for the difference between multi-year and single-year composite means. The confidence levels are described in the figure captions.

Declarations

Data availability

The observation data, COBESST2 and PREC, are available at <https://psl.noaa.gov/data/gridded/data.cobe2.html> and <https://psl.noaa.gov/data/gridded/data.precl.html>. The ORAS4 and ORAS5 datasets are available at <ftp://ftp-icdc.cen.uni-hamburg.de/EASYInit/ORA-S4/> and <https://icdc.cen.uni-hamburg.de/thredds/catalog/ftpthredds/EASYInit/oras5/catalog.html>; GECCO2 at <ftp://ftp-icdc.cen.uni-hamburg.de/EASYInit/GECCO2/>; GFDLECDAv3.1 at <ftp://nomads.gfdl.noaa.gov/2/ECDA/ecda/GFDL-CM2.1-ECDA/>; ERA40 at <https://apps.ecmwf.int/datasets/data/era40-moda/levtype=sfc/>; ERA-Interim at <https://apps.ecmwf.int/datasets/data/interim-full-moda/levtype=sfc/>. The CMIP6 datasets are available at <https://pcmdi.llnl.gov/CMIP6/>

Code availability.

The linear baroclinic model used in this study is available via <https://ccsr.aori.u-tokyo.ac.jp/~lbm/sub/lbm.html>.

Acknowledgments

We would like to thank the modeling groups PCMDI and WCRP's WGCM for their efforts in making the CMIP6 multi-model dataset available. We also thank Tomoki Tozuka for the constructive comments. This work was supported by Grant-in-Aid 26247079 and the Integrated Research Program for Advancing Climate Models (JPMXD0717935457) from the Ministry of Education, Culture, Sports, Science and Technology (MEXT), Japan.

Author contributions

T.I. conducted the research and wrote the manuscript. M.W. advised the analysis and improved the manuscript.

Additional Information

Supplementary information accompanies this paper at XXXXXXXX

Competing financial interests: The authors declare no competing financial interests.

References

1. Jin, F.-F., Neelin, J. D. & Ghil, M. El Niño on the devil's staircase: annual subharmonic steps to chaos. *Science* **264**, 70–72 (1994).
2. Tziperman, E., Stone, L., Cane, M. A. & Jarosh, H. El Niño chaos: Overlapping of resonances between the seasonal cycle and the Pacific ocean-atmosphere oscillator. *Science* **264**, 72–74 (1994).
3. Neelin, J. D., Jin, F.-F. & Syu, H.-H. Variations in ENSO phase locking. *J. Clim.* **13**, 2570–2590 (2000).
4. Jin, F.-F. An equatorial ocean recharge paradigm for ENSO. Part I: conceptual model. *J. Atmospheric Sci.* **54**, 811–829 (1997).
5. Jin, F.-F. An equatorial ocean recharge paradigm for ENSO. Part II: A stripped-down coupled model. *J. Atmospheric Sci.* **54**, 830–847 (1997).
6. Burgers, G. The simplest ENSO recharge oscillator. *Geophys. Res. Lett.* **32**, (2005).
7. Meinen, C. S. & McPhaden, M. J. Observations of warm water volume changes in the equatorial Pacific and their relationship to El Niño to La Niña. *J. Clim.* **13**, 9 (2000).
8. Meinen, C. S. & McPhaden, M. J. Interannual variability in warm water volume transports in the equatorial Pacific during 1993–99. *J. Phys. Oceanogr.* **31**, 1324–1345 (2001).

9. Meinen, C. S. Meridional extent and interannual variability of the Pacific ocean tropical–subtropical warm water exchange. *J. Phys. Oceanogr.* **35**, 323–335 (2005).
10. Timmermann, A. *et al.* El Niño–Southern Oscillation complexity. *Nature* **559**, 535–545 (2018).
11. Cole, J. E. Multiyear La Niña events and persistent drought in the contiguous United States. *Geophys. Res. Lett.* **29**, 1–4 (2002).
12. Harrison, D. E. Monthly mean island surface winds in the central tropical Pacific and El Niño events. *Mon. Weather Rev.* **115**, 3133–3145 (1987).
13. Harrison, D. E. & Vecchi, G. A. On the termination of El Niño. *Geophys. Res. Lett.* **26**, 1593–1596 (1999).
14. McGregor, S., Timmermann, A., Schneider, N., Stuecker, M. F. & England, M. H. The effect of the South Pacific Convergence Zone on the termination of El Niño events and the meridional asymmetry of ENSO. *J. Clim.* **25**, 5566–5586 (2012).
15. McGregor, S. *et al.* Meridional movement of wind anomalies during ENSO events and their role in event termination. *Geophys. Res. Lett.* **40**, 749–754 (2013).
16. Lengaigne, M., Boulanger, J.-P., Menkes, C. & Spencer, H. Influence of the seasonal cycle on the termination of El Niño events in a coupled general circulation model. *J. Clim.* **19**, 1850–1868 (2006).
17. Stuecker, M. F., Timmermann, A., Jin, F.-F., McGregor, S. & Ren, H.-L. A combination mode of the annual cycle and the El Niño/Southern Oscillation. *Nat. Geosci.* **6**, 540–544 (2013).
18. Stuecker, M. F., Jin, F.-F., Timmermann, A. & McGregor, S. Combination mode dynamics of the anomalous northwest Pacific anticyclone. *J. Clim.* **28**, 1093–1111 (2015).
19. DiNezio, P. N. & Deser, C. Nonlinear controls on the persistence of La Niña. *J. Clim.* **27**, 7335–7355 (2014).
20. Park, J.-H. *et al.* Mid-latitude leading double-dip La Niña. *Int. J. Climatol.* 1–18 (2020) doi:10.1002/joc.6772.
21. Luo, J.-J., Liu, G., Hendon, H., Alves, O. & Yamagata, T. Inter-basin sources for two-year predictability of the multi-year La Niña event in 2010–2012. *Sci. Rep.* **7**, (2017).
22. Wu, X., Okumura, Y. M. & DiNezio, P. N. What controls the duration of El Niño and La Niña events? *J. Clim.* **32**, 5941–5965 (2019).
23. Okumura, Y. M., DiNezio, P. & Deser, C. Evolving impacts of multiyear La Niña events on atmospheric circulation and U.S. drought. *Geophys. Res. Lett.* **44**, 11,614–11,623 (2017).
24. Iwakiri, T. & Watanabe, M. Multiyear La Niña impact on summer temperature over Japan. *J. Meteorol. Soc. Jpn. Ser II* **98**, (2020).
25. Barnston, A. G., Tippett, M. K., L'Heureux, M. L., Li, S. & DeWitt, D. G. Skill of Real-Time Seasonal ENSO Model Predictions During 2002–11: Is Our Capability Increasing? *Bull. Am. Meteorol. Soc.* **93**, ES48–ES50 (2012).
26. Ham, Y.-G., Kim, J.-H. & Luo, J.-J. Deep learning for multi-year ENSO forecasts. *Nature* **573**, 568–572 (2020).

27. An, S.-I. & Jin, F.-F. Nonlinearity and asymmetry of ENSO. *J. Clim.* **17**, 2399–2412 (2004).
28. Su, J. *et al.* Causes of the El Niño and La Niña amplitude asymmetry in the equatorial eastern Pacific. *J. Clim.* **23**, 605–617 (2010).
29. Eyring, V. *et al.* Overview of the Coupled Model Intercomparison Project Phase 6 (CMIP6) experimental design and organization. *Geosci. Model Dev.* **9**, 1937–1958 (2016).
30. Jin, F.-F., An, S.-I., Timmermann, A. & Zhao, J. Strong El Niño events and nonlinear dynamical heating. *Geophys. Res. Lett.* **30**, (2003).
31. Zebiak, S. E. Oceanic heat content variability and El Niño cycle. *J. Phys. Oceanogr.* **19**, 475–486 (1989).
32. Clarke, A. J., Van Gorder, S. & Colantuono, G. Wind stress curl and ENSO discharge/recharge in the equatorial Pacific. *J. Phys. Oceanogr.* **37**, 1077–1091 (2007).
33. Ohba, M. & Ueda, H. Role of nonlinear atmospheric response to SST on the asymmetric transition process of ENSO. *J. Clim.* **22**, 177–192 (2009).
34. Cai, W. *et al.* Pantropical climate interactions. *Science* **363**, eaav4236 (2019).
35. Abellán, E. & McGregor, S. The role of the southward wind shift in both, the seasonal synchronization and duration of ENSO events. *Clim. Dyn.* **47**, 509–527 (2016).
36. Chen, D., Cane, M. A., Kaplan, A., Zebiak, S. E. & Huang, D. Predictability of El Niño over the past 148 years. *Nature* **428**, 733–736 (2004).
37. DiNezio, P. N., Deser, C., Okumura, Y. & Karspeck, A. Predictability of 2-year La Niña events in a coupled general circulation model. *Clim. Dyn.* **49**, 4237–4261 (2017).
38. Wang, B. *et al.* Historical change of El Niño properties sheds light on future changes of extreme El Niño. *Proc. Natl. Acad. Sci.* **116**, 22512–22517 (2019).
39. Kim, S. T. *et al.* Response of El Niño sea surface temperature variability to greenhouse warming. *Nat. Clim. Change* **4**, 786–790 (2014).
40. Hirahara, S., Ishii, M. & Fukuda, Y. Centennial-scale sea surface temperature analysis and its uncertainty. *J. Clim.* **27**, 57–75 (2014).
41. Chen, M., Xie, P., Janowiak, J. E. & Arkin, P. A. Global land precipitation: A 50-yr monthly analysis based on gauge observations. *J. Hydrometeorol.* **3**, 18 (2002).
42. Balmaseda, M. A., Mogensen, K. & Weaver, A. T. Evaluation of the ECMWF ocean reanalysis system ORAS4. *Q. J. R. Meteorol. Soc.* **139**, 1132–1161 (2013).
43. Zuo, H., Balmaseda, M. A., Tietsche, S., Mogensen, K. & Mayer, M. The ECMWF operational ensemble reanalysis–analysis system for ocean and sea ice: a description of the system and assessment. *Ocean Sci.* **15**, 779–808 (2019).
44. Köhl, A. Evaluation of the GECCO2 ocean synthesis: transports of volume, heat and freshwater in the Atlantic. *Q. J. R. Meteorol. Soc.* **141**, 166–181 (2015).
45. Chang, Y.-S., Zhang, S., Rosati, A., Delworth, T. L. & Stern, W. F. An assessment of oceanic variability

46. Uppala, S. M. *et al.* The ERA-40 re-analysis. *Q. J. R. Meteorol. Soc.* **131**, 2961–3012 (2005).
47. Dee, D. P. *et al.* The ERA-Interim reanalysis: configuration and performance of the data assimilation system. *Q. J. R. Meteorol. Soc.* **137**, 553–597 (2011).
48. Sato, O. T. & Polito, P. S. Comparison of the global meridional Ekman heat flux estimated from four wind sources. *J. Phys. Oceanogr.* **35**, 94–108 (2005).
49. Watanabe, M. & Kimoto, M. Atmosphere-ocean thermal coupling in the North Atlantic: A positive feedback. *Q. J. R. Meteorol. Soc.* **126**, 3343–3369 (2000).
50. Yanai, M., Esbensen, S. & Chu, J. Determination of bulk properties of tropical cloud clusters from large-scale heat and moisture budgets. *J. Atmospheric Sci.* **30**, 611–627 (1973).

Figures

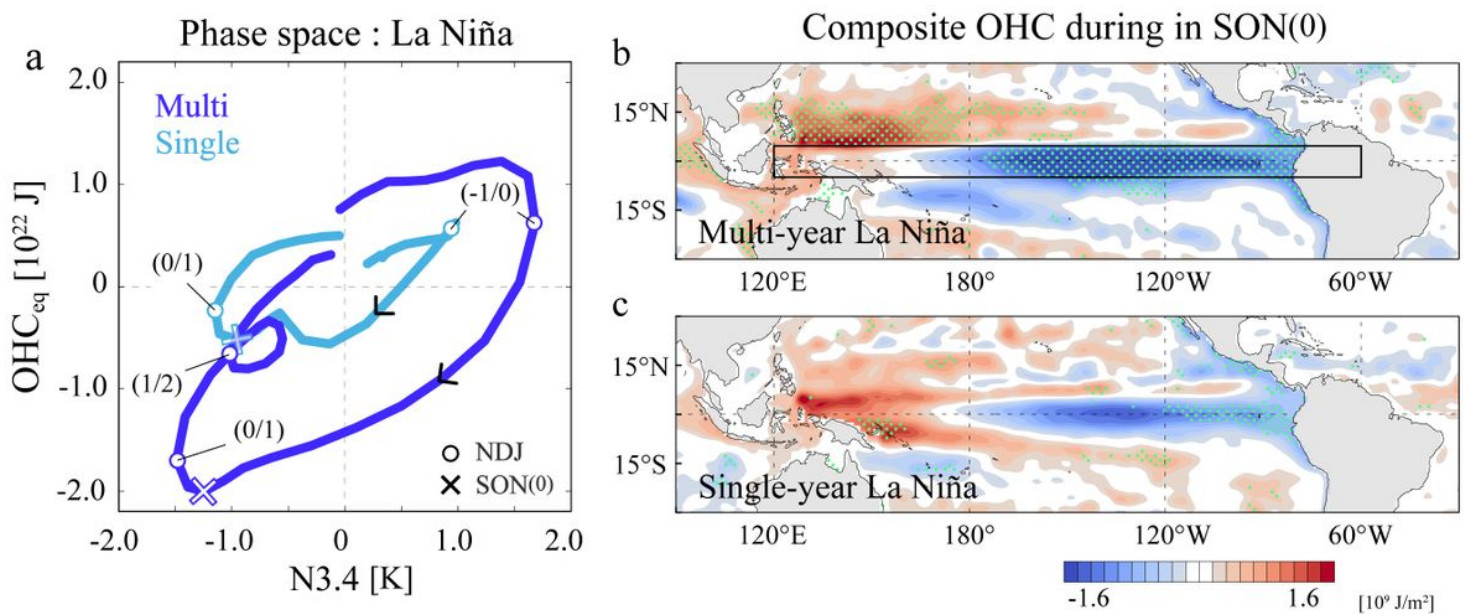


Figure 1

Comparison of the phase transition between multi-year and single-year La Niña. (a) Phase space diagram for observed composite multi-year (blue) and single-year (light blue) La Niña plotted for the periods preceding El Niño to the termination of La Niña. The horizontal axis is N3.4 and the vertical axis is the OHC_{eq} anomaly. The trajectories are smoothed with a three-month running-mean. Circles denote NDJ for each year and crosses denote SON(0). (b,c) Multi-year and single-year La Niña composite maps of OHC anomalies integrated from the surface to 500 m during SON(0), respectively. Dots indicate anomalies statistically significant at the 95% confidence level. The box in (b) represents the region to calculate OHC_{eq}.

COBE-SST2 & ORAS4 [1961-2016]
 Ocean heat transport composite for La Niña

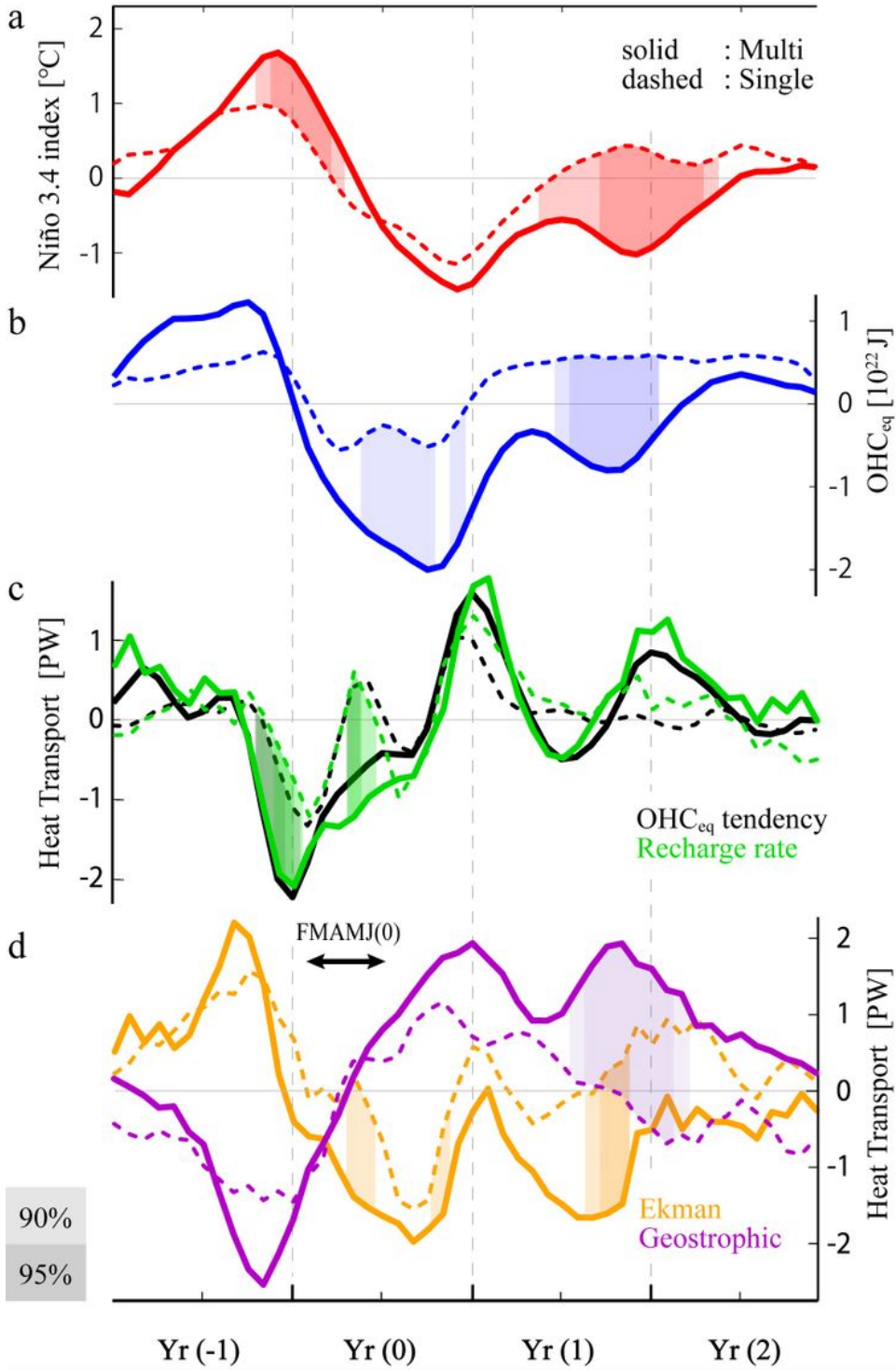


Figure 2

Time evolution of multi-year and single-year La Niña and associated recharge processes. Time series of composited multi-year (solid curves) and single-year (dashed curves) La Niña events for (a) N3.4 and (b) OHC_{eq} anomalies; (c) OHC_{eq} tendency (black) and its reconstruction by the recharge rate (green) (Methods); and (d) contribution to the recharge rate by the geostrophic term (GHT, purple) and the Ekman

difference between multi-year and single-year composites

statistically significant at the 90 and 95 % confidence levels. The time series are smoothed with a three-month running mean after the individual budget term was calculated.

FMAMJ⁽⁰⁾

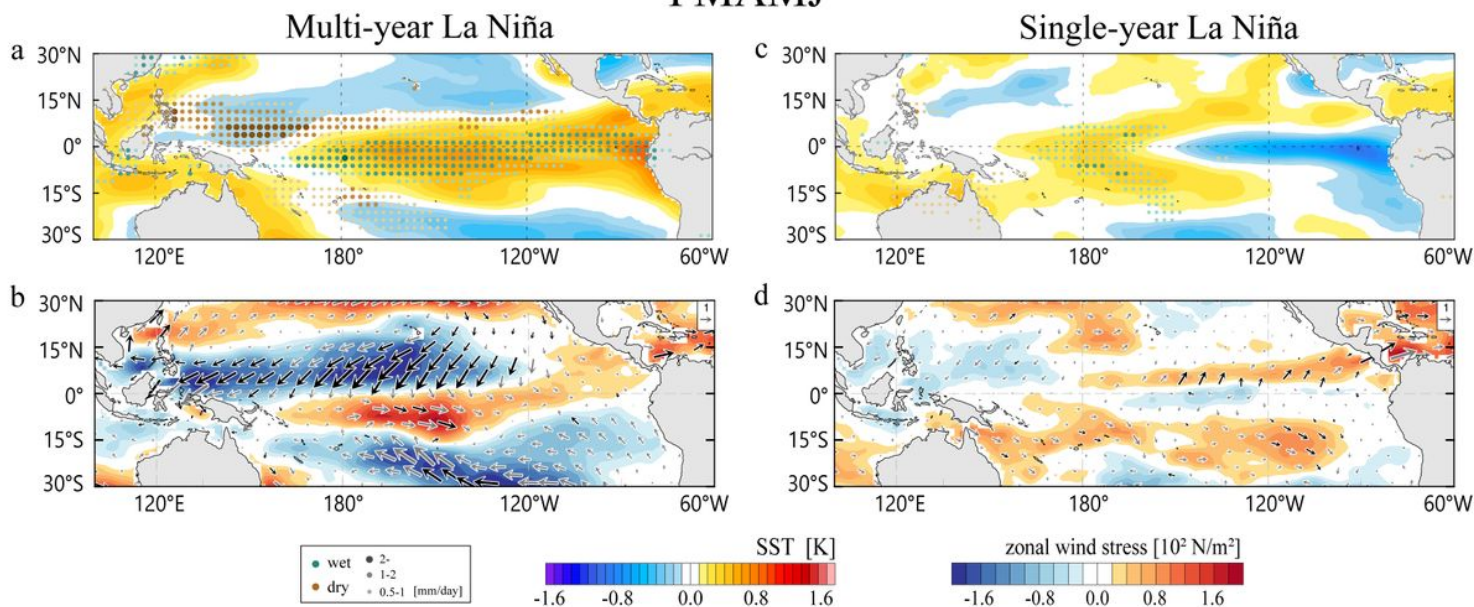


Figure 3

Multi-year and single-year La Niña composite maps in FMAMJ(0). (a) Anomalous SST (shading) and precipitation (dots) and (b) surface zonal wind stress (shading) and wind stress vector (unit in 10^{-2} N/m²) for the multi-year La Niña composite. (c,d) As in (a,b) but for the single-year La Niña composite. Vectors in black indicate anomalies statistically significant at the 95 % confidence level.

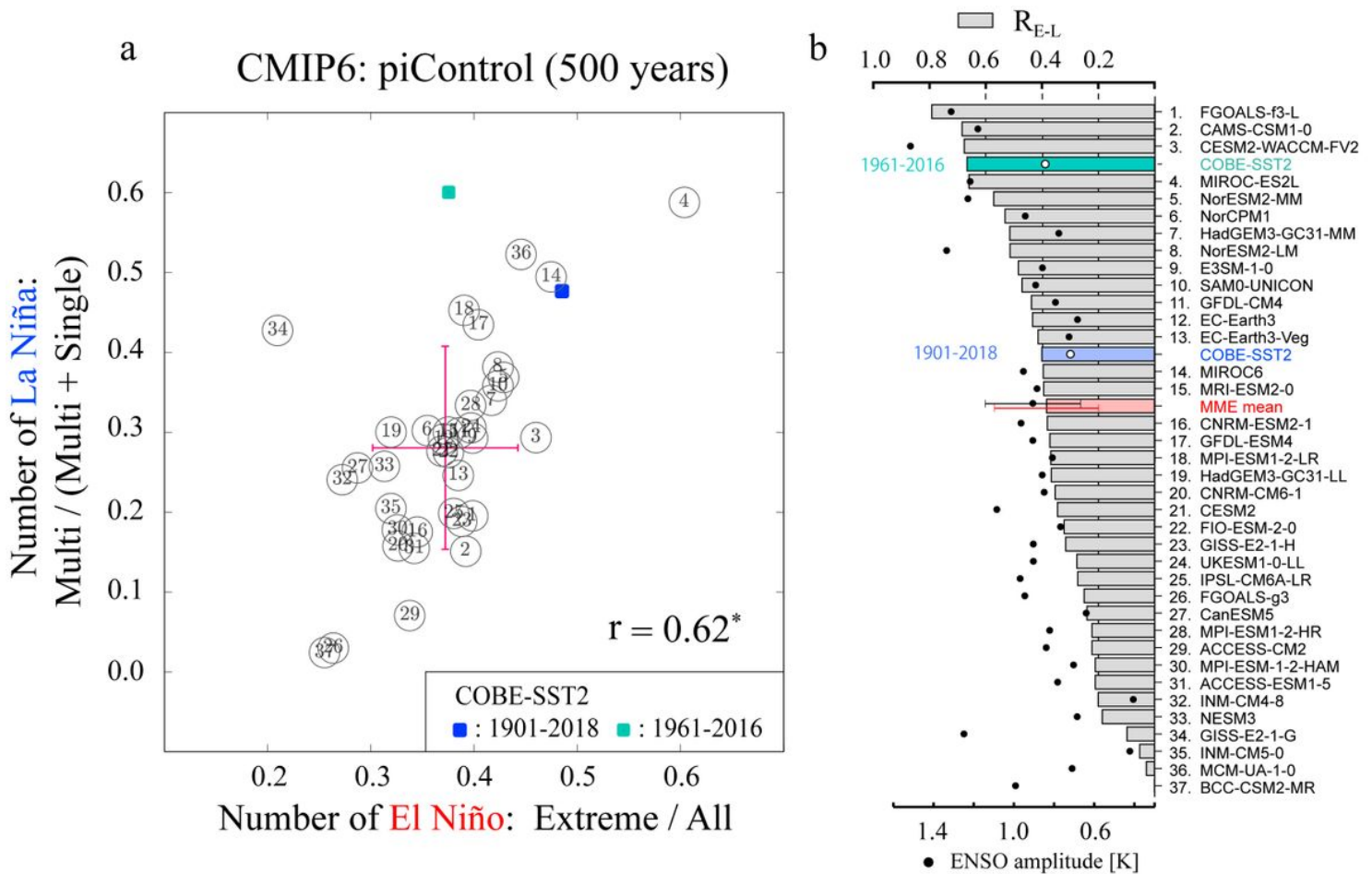


Figure 4

Relationship between the frequency of extreme El Niño and multi-year La Niña in observations and CMIP6 pre-industrial control simulations. (a) The horizontal axis is a ratio of the number of extreme El Niño and all El Niño events. The vertical axis is a ratio of the number of extreme multi-year La Niña and multi-year La Niña events. The correlation coefficient among 37 models is shown at the bottom right. Each number corresponds to the CMIP6 model sorted in (b). (b) R_{E-L} , measuring the coupling between preceding extreme El Niño and multi-year La Niña, in observations and 37 CMIP6 models. Bars indicate R_{E-L} (unitless), and dots show the ENSO amplitude (K). Error bars represent the range of one standard deviation range for all models.

Supplementary Files

This is a list of supplementary files associated with this preprint. Click to download.

- [SupplInfofinal.ng.docx](#)